RESEARCH ARTICLE | NOVEMBER 09 2023

### Room temperature two-dimensional electron gas scattering time, effective mass, and mobility parameters in Al, Ga, N/GaN heterostructures (0.07 $\le x \le 0.42$ )

Sean Knight ■ ⑥; Steffen Richter ⑥; Alexis Papamichail ⑥; Philipp Kühne; Nerijus Armakavicius ⑥; Shiqi Guo ⑥; Axel R. Persson ⑥; Vallery Stanishev ⑥; Viktor Rindert ⑥; Per O. Å. Persson ⑥; Plamen P. Paskov ⑥; Mathias Schubert ⑥; Vanya Darakchieva ■ ⑥



J. Appl. Phys. 134, 185701 (2023) https://doi.org/10.1063/5.0163754





### Articles You May Be Interested In

Impact of AI profile in high-AI content AIGaN/GaN HEMTs on the 2DEG properties

Appl. Phys. Lett. (September 2024)

Electron effective mass in GaN revisited: New insights from terahertz and mid-infrared optical Hall effect

APL Mater. (February 2024)

Enhancement of 2DEG effective mass in  $AIN/AI_{0.78}Ga_{0.22}N$  high electron mobility transistor structure determined by THz optical Hall effect

Appl. Phys. Lett. (June 2022)





# 18 September 2025 16:58:48

## Room temperature two-dimensional electron gas scattering time, effective mass, and mobility parameters in $Al_xGa_{1-x}N/GaN$ heterostructures $(0.07 \le x \le 0.42)$

Cite as: J. Appl. Phys. **134**, 185701 (2023); doi: 10.1063/5.0163754 Submitted: 19 June 2023 · Accepted: 12 October 2023 · Published Online: 9 November 2023







```
Sean Knight, <sup>1,2,3,a)</sup> Steffen Richter, <sup>1,2,3</sup> Alexis Papamichail, <sup>1,2</sup> Philipp Kühne, <sup>1,2</sup> Nerijus Armakavicius, <sup>1,2</sup> Shiqi Guo, <sup>1,2</sup> Axel R. Persson, <sup>1,4</sup> Vallery Stanishev, <sup>1,2</sup> Viktor Rindert, Per O. Å. Persson, Plamen P. Paskov, Mathias Schubert, <sup>2,3,5</sup> and Vanya Darakchieva, <sup>1,2,3,a</sup>
```

### **AFFILIATIONS**

- <sup>1</sup>Center for III-Nitride Technology (C3NiT—Janzén), Department of Physics, Chemistry and Biology (IFM), Linköping University, 581 83 Linköping, Sweden
- <sup>2</sup>Terahertz Materials Analysis Center (THeMAC), Department of Physics, Chemistry and Biology (IFM), Linköping University, 581 83 Linköping, Sweden
- <sup>3</sup>Solid State Physics and NanoLund, Lund University, 22100 Lund, Sweden
- <sup>4</sup>Thin Film Physics Division, Department of Physics, Chemistry and Biology (IFM), Linköping University, 581 83 Linköping, Sweden
- <sup>5</sup>Department of Electrical and Computer Engineering, University of Nebraska-Lincoln, Lincoln, Nebraska 68588, USA

a) Authors to whom correspondence should be addressed: sean.knight@liu.se and vanya.darakchieva@ftf.lth.se

### **ABSTRACT**

 $Al_xGa_{1-x}N/GaN$  high-electron-mobility transistor (HEMT) structures are key components in electronic devices operating at gigahertz or higher frequencies. In order to optimize such HEMT structures, understanding their electronic response at high frequencies and room temperature is required. Here, we present a study of the room temperature free charge carrier properties of the two-dimensional electron gas (2DEG) in HEMT structures with varying Al content in the  $Al_xGa_{1-x}N$  barrier layers between x=0.07 and x=0.42. We discuss and compare 2DEG sheet density, mobility, effective mass, sheet resistance, and scattering times, which are determined by theoretical calculations, contactless Hall effect, capacitance-voltage, Eddy current, and cavity-enhanced terahertz optical Hall effect (THz-OHE) measurements using a low-field permanent magnet (0.6 T). From our THz-OHE results, we observe that the measured mobility reduction from x=0.13 to x=0.42 is driven by the decrease in 2DEG scattering time, and not the change in effective mass. For x<0.42, the 2DEG effective mass is found to be larger than for electrons in bulk GaN, which in turn, contributes to a decrease in the principally achievable mobility. From our theoretical calculations, we find that values close to  $0.3m_0$  can be explained by the combined effects of conduction band nonparabolicity, polarons, and hybridization of the electron wavefunction through penetration into the barrier layer.

© 2023 Author(s). All article content, except where otherwise noted, is licensed under a Creative Commons Attribution (CC BY) license (http://creativecommons.org/licenses/by/4.0/). https://doi.org/10.1063/5.0163754

### I. INTRODUCTION

 $Al_xGa_{1-x}N/GaN$  high-electron-mobility transistors (HEMTs) are important components in modern high-power and high-frequency electronics. In order to enhance their output power

capability and increase maximum oscillation frequencies beyond 250 GHz, a thorough understanding of the two-dimensional electron gas (2DEG) properties in the channel formed at the AlGaN/GaN interface is required. Since both the HEMT

constituent materials and 2DEG transport govern device performance, it is crucial to study how variations in basic parameters, such as Al composition x, affect heterostructure growth and the resulting 2DEG properties. The formation of a 2DEG at wurtzite  $Al_xGa_{1-x}N/GaN$  interfaces is enabled by the spontaneous and piezoelectric polarization, where the latter is determined by strain in pseudomorphic growth of the  $Al_xGa_{1-x}N$  barrier layer.<sup>2–5</sup> Electrons accumulate at the interface and form a 2DEG as a consequence of strong polarization and band offsets between GaN and  $Al_xGa_{1-x}N$ .<sup>2,3,6</sup> A key parameter for tuning HEMT characteristics is the Al content x in the  $Al_xGa_{1-x}N$  barrier layer, which heavily influences the magnitude of the polarization fields, pseudomorphic growth quality, and 2DEG sheet density.<sup>2–4,7–14</sup>

The most critical property of HEMTs which determines high-frequency performance is the 2DEG mobility,  $\mu$ . At room temperature, maximum mobilities have been found near x=0.17 as a result of various competing scattering mechanisms. <sup>15-18</sup> The highest reported room temperature values for  $\mu$  are between 2200 and 2400 cm²/V s, obtained for AlGaN/GaN-based HEMTs with smooth and abrupt interfaces. <sup>19-22</sup> A typical way to achieve high mobilities is by incorporating a thin ( $\approx$ 1 nm) AlN interlayer between the barrier and channel layers, which reduces interface scattering, prevents trapping of hot electrons in the AlGaN or at surface states, and improves the 2DEG confinement. In fact, we have recently demonstrated a 2DEG mobility of (2370  $\pm$  25) cm²/V s in an Al<sub>x</sub>Ga<sub>1-x</sub>N/AlN/GaN HEMT with Al content of x=0.3. <sup>23</sup>

Both electrical and optical methods have been exploited to assess the 2DEG parameters in  $Al_xGa_{1-x}N/GaN$  heterostructures. Commonly, 2DEG mobility and sheet carrier density are obtained from electrical direct-current (DC) Hall effect measurements, which require the fabrication of electrical contacts. Contactless methods permit testing of structures without need for full device processing.2 <sup>7</sup> The optical Hall effect (OHE) is a contactless method for studying 2DEG properties in such semiconductor heterostructures. The OHE technique measures the change in polarization of light due to the interaction with free charge carriers subjected to an external magnetic field at infrared (IR) or terahertz (THz) frequencies by employing spectroscopic ellipsometry.26 Upon matching calculated OHE data to measured OHE data, one can obtain the charge carrier density, mobility, and effective mass parameters, including their anisotropy in bulk as well as 2D free charge carrier systems. 21,33,34 The significance of the OHE is that the 2DEG effective mass parameter can be extracted, which along with density and mobility, allows for improved understanding of 2DEG transport within the heterostructures.

Although the fundamental principles of the electron effective mass in GaN and AlGaN epitaxial layers are well known, additional factors should be considered for the 2DEG effective mass in AlGaN/GaN-based HEMT structures. Since the 2DEG is confined in the GaN channel at the Al<sub>x</sub>Ga<sub>1-x</sub>N/GaN interface, the electron effective mass parameter  $m^*$  of bulk GaN arguably has the strongest influence on the 2DEG  $m^*$ . For bulk-like wurtzite GaN, a slightly anisotropic room temperature electron effective mass has been found, with  $m^*_{\perp} = (0.237 \pm 0.006) m_0$  in the direction perpendicular to the c axis, and  $m^*_{\parallel} = (0.228 \pm 0.008) m_0$  in the direction

parallel to the c axis, where  $m_0$  is the free electron mass.<sup>35</sup> However, an isotropically averaged value of  $m^* \approx 0.22m_0$  has been commonly adopted for *n*-type GaN.<sup>36</sup> Since penetration of the electron wavefunction into the barrier is expected, the electron effective mass in bulk  $Al_xGa_{1-x}N$  should be considered as well. The  $m^*$ parameter of bulk-like Al<sub>x</sub>Ga<sub>1-x</sub>N thin films has been studied at room temperature and can be linearly interpolated between  $m_{GaN}^* = 0.232 \, m_0$  and  $m_{AlN}^* = 0.364 \, m_0^{29}$  Regarding  $m^*$  values determined for 2DEGs, various studies exist which report effective masses different from  $m^* = 0.22m_0$  for bulk GaN. A previous investigation of 2DEG confinement effects in AlGaN/GaN heterostructures by electrical Hall effect and Shubnikov-de Haas (SdH) effect measurements found that a dominant influence on  $m^*$  was penetration of the electron wavefunction from the GaN channel into the AlGaN barrier.<sup>37</sup> This hybridized effective mass contribution was claimed to be even stronger than the effect of band nonparabolicity,<sup>37</sup> which otherwise often governs effective mass enhancement in 2DEGs. 16,38,39 An additional increase of the 2DEG effective mass due to the polaron effect is expected.<sup>37,40</sup> A further, although smaller, 2DEG effective mass increase could be expected at high magnetic fields due to field-induced nonparabolicity.<sup>4</sup> Prior THz-OHE and THz time-domain spectroscopy (THz-TDS) investigations on  $Al_xGa_{1-x}N/GaN$  HEMT structures have found  $m^*$ parameters at room temperature being larger than the bulk value for GaN. 21,33,42,43 It is worth noting that the electron effective mass obtained from cyclotron resonances or SdH oscillations requires high mobilities and consequently is often limited to low temperatures. In many previous reports, low temperature 2DEG  $m^*$  values were found smaller than the value for bulk GaN at room get temperature.  $^{17,37,41,41,44-47}$  Other works reported values close to the bulk value for GaN. 16,48-50

Knowledge of  $m^*$  in addition to 2DEG mobility gives access to the Drude scattering time  $\tau$ . This parameter separation is important in determining the mechanisms involved in mobility reduction, i.e., shorter scattering times or enhanced effective masses. Despite existing earlier investigations of the 2DEG at  $Al_xGa_{1-x}N/GaN$  interfaces, a systematic study for the dependence of  $m^*$  and  $\tau$  as a function of Al content in the  $Al_xGa_{1-x}N$  barriers is still lacking. Similarly, considerations at room temperature are rare, despite the fact that typical HEMTs operate at room or elevated temperatures. These two aspects render the present work distinct from investigations that only employ electrical Hall effect or low-temperature methods, such as cyclotron resonance and SdH effect.

In this work, we present a room temperature investigation of the 2DEG properties in  ${\rm Al}_x{\rm Ga}_{1-x}{\rm N/Ga}{\rm N}$  HEMT structures with varying Al content, x, between x=0.07 and x=0.42 in the barrier. Terahertz optical Hall effect (THz-OHE) measurements and analysis were performed to determine the sheet electron density  $N_{\rm s}$ , scattering time  $\tau$ , and  $m^*$  parameters using the classical quasi-free electron (Drude) model approximation, as well as the optical mobility  $\mu$  using the linear carrier-momentum-relaxation approximation model as a function of x. We compare our findings to results from electrical and contactless measurements and discuss within the context of existing data. The distinction between  $m^*$  and  $\tau$  enables a more comprehensive evaluation of 2DEG mobility limitations than could be gained by other methods.

### II. THEORY

### A. Optical Hall effect

The procedure for analyzing OHE data consists of fitting appropriate optical model parameters until a match is achieved between experimental and calculated data. Our model calculations use a 4 × 4 transfer matrix formalism within which every sample constituent is described by a characteristic algebraic element.<sup>5</sup> Every element is constructed from its dielectric function tensor properties and its geometrical thickness parameter. Therefore, the OHE model also requires parameters for thickness of substrate, epitaxial layers, and cavity as well as the anisotropic dielectric function parameters of all sample constituents. Then, the effect of the free charge carriers is augmented by adding the magnetooptic Drude contributions to the tensor of the thin layer which represents the 2D channel within the sample model structure. The contribution of free charge carriers subjected to an external magnetic field  $\mathbf{B} = (b_x, b_y, b_z)$  to the dielectric function tensor can then be constructed within the laboratory Cartesian frame x-y-z. For the case when B is aligned parallel/antiparallel to the z direction, i.e.,  $\mathbf{B} = (0, 0, \pm b_z)$ , this contribution can be written as

$$\boldsymbol{\varepsilon}^{\text{FC-MO}}(\omega) = \begin{pmatrix} \boldsymbol{\varepsilon}_{xx} & i\boldsymbol{\varepsilon}_{xy} & 0 \\ -i\boldsymbol{\varepsilon}_{xy} & \boldsymbol{\varepsilon}_{xx} & 0 \\ 0 & 0 & \boldsymbol{\varepsilon}_{zz} \end{pmatrix}. \tag{1}$$

Assuming for simplicity an isotropic electron effective mass  $m^*$  and mobility  $\mu$ , the symmetric tensor elements  $\varepsilon_{xx}$  and  $\varepsilon_{zz}$  and antisymmetric element  $\varepsilon_{xy}$  become

$$\varepsilon_{xx}(\omega) = -\omega_{p}^{2} \frac{\omega + i\gamma_{p}}{\omega[(\omega + i\gamma_{p})^{2} - \omega_{c}^{2}]},$$
 (2)

$$\varepsilon_{zz}(\omega) = -\omega_{\rm p}^2 \frac{1}{\omega(\omega + i\gamma_{\rm p})},$$
 (3)

$$\varepsilon_{xy}(\omega) = -\omega_{\rm p}^2 \frac{\omega_{\rm c}}{\omega[(\omega + i\gamma_{\rm p})^2 - \omega_{\rm c}^2]},\tag{4}$$

with the plasma frequency  $\omega_{\rm p}^2=(Ne^2)/(\varepsilon_0 m^*)$ , the cyclotron frequency  $\omega_{\rm c}=(qB)/(m^*)$ , and the plasma broadening  $\gamma_{\rm p}=(e)/(\mu m^*)$ . Here, N is the volume free charge carrier density,  $\varepsilon_0$  is the vacuum permittivity, e is the elementary charge, and q=-e is the electron charge. Note, the broadening parameter  $\gamma_{\rm p}$  can be replaced with the scattering time  $\tau=1/\gamma_{\rm p}$ .

For the situation of an ultra-thin free charge carrier channel, e.g., for the 2DEG formed at the interface of the AlGaN barrier layer, the thickness parameter d cannot be obtained from the same OHE model analysis. This is associated with the so-called ultra-thin film limit when the probing wavelength is much larger than the thickness of a given layer<sup>53</sup> as in the case for THz frequencies with millimeter wavelengths compared to few nanometer channel extension in this work. In this limit, the thickness parameter d and the dielectric function  $\varepsilon$  of a given layer are infinitely correlated and cannot be differentiated, while their product  $d\varepsilon$  can be accurately determined from best-match model calculations of ellipsometry

data. Therefore, one can introduce the free charge carrier sheet density,  $N_s = Nd$ , which can then be accurately determined from best-match model calculations when matching OHE measurements. In practice, this is performed by setting the optical model layer thickness of the 2D channel to 1 nm. As a result, model parameter N in Eq. (1) then appears as  $N_s$  in units of cm<sup>-2</sup> when units of  $\omega$ and  $\gamma_{\rm p}$  are cm $^{-1}$ , and q,  $m_0$ ,  $\varepsilon_0$ , B are computed in conventional SI units. Thereby, the results of an OHE experiment performed on 2D free charge carrier channels are parameters  $N_s$ ,  $\mu$ , and  $m^*$ . We note that this procedure for transforming bulk 3D properties into properties corresponding to a 2DEG (3D approximation) is based on assumptions of the validity of the classical Drude model. In this context, we adopt the long wavelength limit in the Lindhard 54 dielectric function as a description of the 2DEG response and therefore ignore the Fermi wave vector dependence of the plasma frequency. Likewise, a classical treatment of spatial dispersion in the isotropic free carrier plasma due to carrier-carrier interaction (carrier gas "pressure") leads to a wave vector dependence of the dielectric function. We argue here that we consider the 2DEG density as a non-interacting carrier gas and therefore also ignore spatial dispersion in the classical isotropic plasma.<sup>56</sup> It is further noted that due to the polar nature of GaN and the relatively large energy of optical phonons with respect to subband energy separation, our 3D approximation is a valid approach to describe 2DEG parameters at high temperatures. 18 However, an extension of our model to account for the wave-vector dependence of the dielectric function derived from the Lindhard formula for the 2D case is of general interest and should be further explored.

Since the magnetic field induced terms in Eq. (1) are directly cortional in sign and magnitude to vector **B**, it is preferable to proportional in sign and magnitude to vector B, it is preferable to perform OHE measurements at strong magnetic fields which are obtained using superconducting magnets. However, such instruments are expensive and measurements require long preparation of times. Alternatively, cavity-enhanced methods make use of interference enhancement effects of the magnetic field induced birefrin-Fabry-Pérot resonances enhance the signatures caused by the magnetooptic effects, and thereby enhance sensitivity to the cyclotron frequency parameter. This enhancement permits to reduce the magnetic field and implement simpler measurement setups. In such configurations, cost efficient permanent magnets can be placed in close proximity to the sample. The field direction can be reversed by replacing the magnet with opposite face toward the sample and repeating the OHE measurement. This mode of cavity-enhanced OHE measurement is performed in this work. It is demonstrated that simple, cheap permanent magnets lead to successful detection of the OHE at THz frequencies and at room temperature.

### B. Hall effect at lower frequencies

Regarding measurements of the Hall effect phenomenon at frequencies below the THz range, both electrical and quasi-optical techniques can be utilized. To probe a material's electrical response at  $\omega=0$ , steady-state DC electrical Hall effect measurements can be performed. For measurements in the lower-gigahertz range, a method referred to as contactless Hall effect can be employed. This nondestructive, quasi-optical technique was used in our

investigations to extract information about the 2DEG parameters, which complements the THz-OHE results. The analysis of such Hall effect measurements obtained at lower frequencies is usually dealt with in terms of the conductivity tensor  $\sigma(\omega)$ , which is nondivergent at zero frequency. Using  $\boldsymbol{\varepsilon} = \mathbf{I} + (i\boldsymbol{\sigma})/(\varepsilon_0\omega)$ , the permittivity tensor form can be rewritten as the complex-valued, frequency-dependent optical conductivity tensor.<sup>26</sup> In the absence of an external magnetic field and at zero frequency, the contribution from free charge carriers to the optical conductivity is rendered  $\sigma^{FC}(\omega = 0) = e\mu N$ . Therefore, knowledge of the conductivity at lower frequencies also provides access to N and  $\mu$ . However, separation of the parameters N,  $\mu$ , and  $m^*$  (or  $\omega_p$ ,  $\omega_c$ , and  $\gamma_p$ ) remains unattainable when techniques such as traditional electrical Hall effect are employed.

### C. Poisson-Schrödinger solution and electron effective mass parameter

Band bending and charge distribution of all layer structures were modeled using a numerical Poisson-Schrödinger (P-S) solver by Snider. 60,61 The Al<sub>x</sub>Ga<sub>1-x</sub>N/GaN interface is modeled by a gradual compositional change over 2 nm, according to experimental results from high-resolution transmission electron microscopy in combination with energy dispersive x-ray spectroscopy as shown in Fig. 2. The calculated electron density profile N is used to compute a hybridized electron effective mass according to 37

$$m_{hyb}^{\star} = \left(\frac{f_{barrier}}{m_{Al_xGa_{1-x}N}^{\star}} + \frac{f_{channel}}{m_{GaN}^{\star}}\right)^{-1},\tag{5}$$

where  $f_{barrier}$  and  $f_{channel}$  are the fractions of the total electron volume density located in the Al<sub>x</sub>Ga<sub>1-x</sub>N barrier and relevant portion of the channel region, respectively,  $f_{barrier} + f_{channel} = 1.$ 

Additionally, we consider effective electron mass parameter enhancement effects due to conduction-band nonparabolicity by using Ando's formula,16,3

$$\frac{m_{nonparabol}^*}{m^*} \approx \sqrt{1 + \frac{4(\frac{E_0}{3} + E_F)}{E_G, GaN}},\tag{6}$$

where  $E_G$ ,  $G_{GaN} = 3.42 \text{ eV}$  is the bandgap energy, and  $E_0$  and  $E_F$  are, respectively, the energy of the ground state in the triangular quantum well at the interface, and the Fermi level with respect to the conduction band minimum (potential minimum) which depend on the considered structure.

Furthermore, we consider effective mass parameter enhancement due to the polaron effect,6

$$\frac{m_{polaron}^{*}}{m^{*}} \approx 1 + \frac{\alpha}{6} + 0.025\alpha^{2} \approx 1.086,$$
 (7)

with Fröhlich coupling constant  $\alpha = 0.48$  for GaN.<sup>63</sup> In contrast to the models for hybridization and nonparabolicity, the polaron effect enhancement ratio is calculated purely as a bulk effect in GaN, and therefore is unchanged as a function of Al content in the barrier. For all models, simulations are performed using the isotropically averaged values of m\* for bulk-like Al<sub>x</sub>Ga<sub>1-x</sub>N given in Ref. 29, i.e., the linear interpolation between  $m_{GaN}^* = 0.232 m_0$  and  $m_{AlN}^* = 0.364 \, m_0$ . Further model calculation details and implemented parameters are described in the supplementary material.

### **III. SAMPLES AND METHODS**

The AlGaN/GaN HEMT structures were grown epitaxially by hot-wall metal-organic chemical vapor deposition (MOCVD) on semi-insulating 4H-SiC (0001).<sup>23</sup> A schematic is shown in the inset in Fig. 1. After a 65 nm thick AlN nucleation layer, about 1 µm relaxed GaN was grown, followed by an approximately 30 nm thick pseudomorphic  $Al_xGa_{1-x}N$  barrier layer. The Al content x was varied between 0.07 and 0.42 by changing the relative amount of trimethylaluminum precursor in the metalorganic precursors gas phase ratio. Nine samples were grown in total (x = 0.07, 0.11, 0.13,0.15, 0.18, 0.21, 0.26, 0.30, 0.42). We note that these  $Al_xGa_{1-x}N/$ GaN heterostructures were intentionally grown without an AlN interlayer in order to evaluate the direct effect of Al content in the barrier layer on the 2DEG properties.

The crystalline quality of the epitaxial layers as well as the Al content and strain state in the barrier layers were evaluated by high resolution x-ray diffraction (HR-XRD) measurements using a triple axis configuration on a PANalytical Empyrean diffractometer. Reciprocal space maps (RSMs) were recorded around the GaN

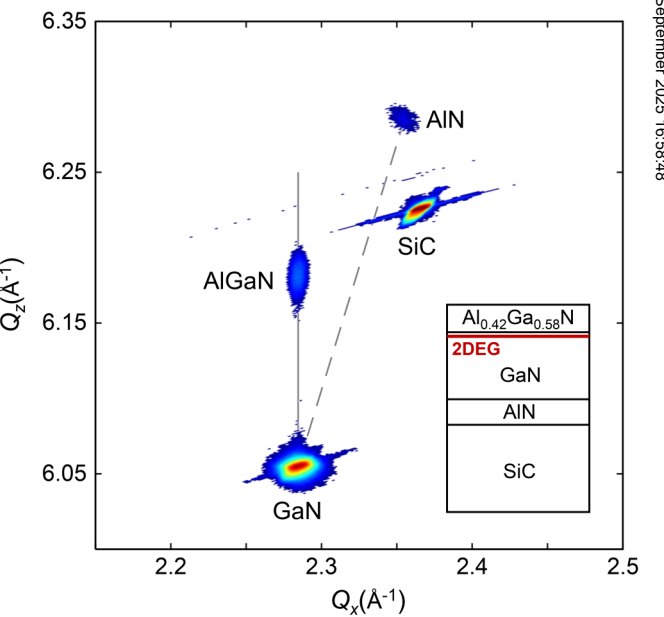


FIG. 1. Reciprocal space map (logarithmic intensity scaling) around the 1015 lattice point for the sample with the Al<sub>0.42</sub>Ga<sub>0.58</sub>N barrier layer, showing pseudomorphic growth of AlGaN on GaN. The solid and dashed gray lines represent the positions expected for pseudomorphic and fully relaxed Al<sub>x</sub>Ga<sub>1-x</sub>N with varying x, respectively. The inset displays a schematic of the HEMT structure. All structures are c-plane oriented and metal-polar.

1015 reciprocal lattice point, using the diffractometer in the two-axis mode and the detector in the scanning line mode. In this case, no analyzer was placed in front of the detector. The extracted lattice constants of the  $Al_xGa_{1-x}N$  were used to determine the Al content by assuming validity of Vegard's rule for the composition dependence of the lattice constants and the elastic stiffness constants.64

Spectroscopic ellipsometry (SE) measurements were performed for all samples using a J. A. Woollam RC2-XI ellipsometer in the spectral range of 0.7-5.9 eV at angles of incidence 40°, 50°, 60°, and 70°. Both the thickness parameters of the  $Al_xGa_{1-x}N$ layers and the lowest band-to-band transition energies (bandgap energy) were determined from the best-match model analysis. Assuming Vegard's rule for the composition dependence of the bandgap energy, x values for the barrier layers were also obtained.

The surface morphology and the root-mean-square (RMS) roughness of the samples were investigated by atomic force microscopy (AFM) using a Veeco Dimension 3100 scanning probe microscope in tapping mode.

The interface quality was investigated by high-angle annular dark-field (HAADF) scanning transmission electron microscopy (STEM) together with energy dispersive X-ray spectroscopy (EDX). The investigation employed the Linköping University double corrected FEI Titan<sup>3</sup> 60-300 operated at 300 kV with the built-in Super-X EDX system. EDX quantifications were made using the built-in software.

THz-OHE measurements were performed at room temperature using a permanent magnet with a field of  $\pm 0.6 \,\mathrm{T}$  at the sample surface. We employed our in-house-built ellipsometer instrument<sup>66</sup> to acquire the upper-left  $3 \times 3$  block of the  $4 \times 4$ Mueller matrix from 720 to 950 GHz in increments of 1.5 GHz. All Mueller matrix data have been normalized by the total reflection at each frequency  $(M_{11})$ . For all acquired THz-OHE data, the angle of incidence was  $45^{\circ}$ , and the sample-to-magnet air gap was fixed to approximately 100 µm using adhesive spacers. Measurements were carried out for both directions of the magnetic field, parallel and anti-parallel to the sample surface. All THz-OHE data were acquired and analyzed using WVASE (J.A. Woollam Co., Inc.). For further details of OHE data acquisition and analyses, we refer to our previous works. 21,26,31,57,

Contactless Hall effect measurements at 10 GHz radiation (Semilab/Lehighton LEI 1610) were carried out to independently obtain mobility and sheet carrier density.59

Hg-probe capacitance-voltage (C-V) measurements (Agilent 4284A) and contactless Eddy current measurements (Eichhorn + Hausmann MX 604) were carried out to independently obtain charge carrier densities N and sheet resistance  $R_s$ , respectively.

Further details on the AFM, SE, XRD-RSM, THz-OHE, and C-V characterizations are found in the supplementary material.

### IV. EXPERIMENTAL RESULTS

### A. Structural properties

Results from AFM investigations are shown in the supplemental material together with the values for x and layer thicknesses obtained by XRD and SE. For all samples with  $0.07 \le x \le 0.42$ , we observe high epitaxial layer quality without cracks and with RMS surface roughness between 0.2 and 0.4 nm over sampling areas of  $5\times5\,\mu\text{m}^2$ . The smooth surface of the thin AlGaN barrier layer is indicative for a high quality of the Al<sub>x</sub>Ga<sub>1-x</sub>N/GaN interface.

Figure 1 shows the 1015 lattice point RSM for the HEMT structure with the highest Al content revealing fully pseudomorphic growth. From evaluating the broadening of rocking curves for multiple Bragg reflections, 70,71 typical dislocation densities are estimated to be below  $7 \times 10^7$  cm<sup>-2</sup> for screw- and below  $6 \times 10^8$  cm<sup>-2</sup> for edge-type dislocations. The expected critical thickness value for pseudomorphic growth at x = 0.42 is around or below 15 nm. For our 30 nm thick Al<sub>x</sub>Ga<sub>1-x</sub>N layers, the critical thickness should be exceeded already at x about 0.2–0.3.<sup>5,72</sup> We suggest that the reason why we obtained crack-free Al<sub>x</sub>Ga<sub>1-x</sub>N layers on GaN is a compositional grading across the GaN/Al<sub>x</sub>Ga<sub>1-x</sub>N interface as revealed by TEM (Fig. 2).

Figure 2 depicts representative results from EDX and HAADF-STEM investigations across the Al<sub>x</sub>Ga<sub>1-x</sub>N/GaN interface of the sample with x = 0.15. The intensity variations of both the relative Al-to-Ga signal as well as the integrated image intensity reveal a sharp transition between the GaN and AlGaN layers, which is observed to occur within approximately 2 nm.

### B. 2DEG properties: THz-OHE, contactless Hall effect, C-V, and Eddy current results

Figure 3 shows selected THz-OHE data presented as differences between measurements at positive and negative magnetic field directions  $(\Delta M_{ij} = M_{ij}^+ - M_{ij}^-)$ . The Mueller matrix data of reflect the magnetic field and spectral dependencies of the anisot-group in the dielectric tensor, as described in Eqs. (2)–(4). Specifically, the off diagonal elements in Eq. (4) are proportional to the cyclotron frequency and provide most sensitivity to this

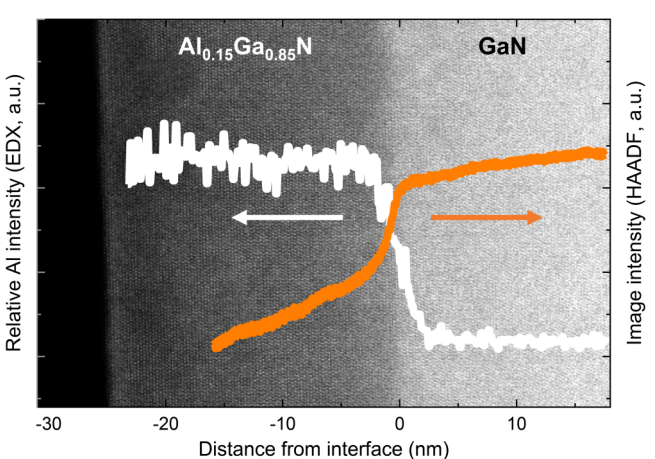
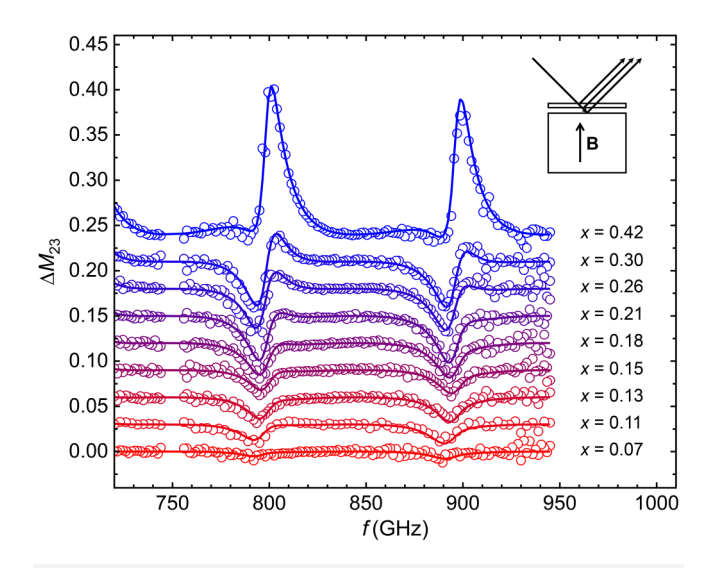


FIG. 2. EDX Al/Ga signal (white line) and HAADF-STEM integrated intensity profile (orange line) as a function of distance from the Al<sub>x</sub>Ga<sub>1-x</sub>N/GaN interface for the HEMT structure with x = 0.15. The HAADF-STEM image is shown in the background with the intensity variations directly coupled to the local value of x. The Al<sub>x</sub>Ga<sub>1-x</sub>N/GaN interface thickness is graded linearly within approximately 2 nm.



**FIG. 3.** THz-OHE experimental (open circles) and best-model (solid lines) difference-spectra for the  ${\rm Al_xGa_{1-x}N/GaN}$  HEMT structures with varying Al composition,  ${\rm x}$ . Difference-data  $\Delta M_{ij}$  are calculated by subtracting Mueller matrix elements measured with positive  $(M_{ij}^+)$  and negative  $(M_{ij}^-)$  magnetic field directions for each HEMT sample in the set. Only  $\Delta M_{23}$  is shown here. Individual lines are vertically offset by 0.03 for clarity. The upper-right diagram illustrates the principle of cavity-enhanced THz-OHE, in which the incident THz radiation reflects off of the sample surface, sample backside interface, and the permanent magnet surface to ultimately interfere in the outgoing beam, thereby enhancing the signal-to-noise ratios.

parameter. Note that the Mueller matrix element differences between positive and negative fields equal zero in the case of no free charge carriers. When the permanent magnet's field is applied, the 2DEG becomes magnetooptically birefringent due to the force induced by B. Therefore,  $\Delta M_{13}$ ,  $\Delta M_{23}$ ,  $\Delta M_{31}$ ,  $\Delta M_{32}$  elements are most representative of the OHE and are highlighted here. See also the supplementary material. The features observed in the Mueller matrix difference spectra are caused by differences between left and right circularly polarized light propagation due to magnetooptic anisotropy of the 2DEG. The differences are enhanced by substrate and sample-magnet cavity Fabry-Pérot interference resonances and thus enhance the OHE signal.<sup>57,58</sup> In this experimental configuration, the OHE difference spectra are highly sensitive to the HEMT structure's 2DEG properties. This enables the extraction of the desired parameters using the line shape analysis procedure described above. All THz-OHE data for each sample are analyzed simultaneously to produce the best-model data (solid lines: Fig. 3). The resulting parameter values for  $N_s$  (Fig. 4),  $m^*$  (Fig. 6), and  $\mu$  (Fig. 7) are discussed further below. Due to limited sensitivity to the 2DEG response perpendicular to the sample surface plane, the out-of-plane  $m^*$  and  $\mu$  parameters were coupled to the in-plane values during our OHE model analysis. Therefore, these values of  $m^*$ ,  $\mu$ , and  $\tau$  should be regarded as isotropically averaged.

As seen in Fig. 3 and also in the supplementary material for all other Mueller matrix element difference spectra, the OHE

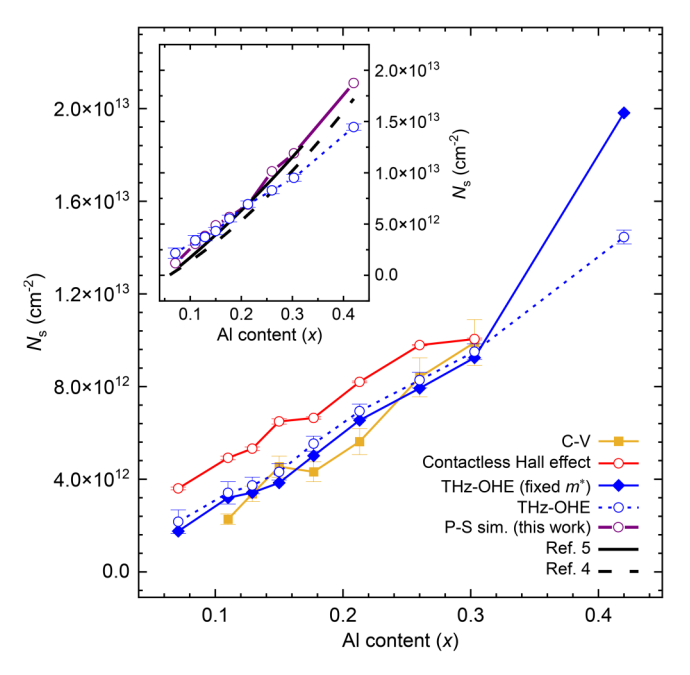


**FIG. 4.** Sheet density  $N_{\rm s}$  obtained by THz-OHE (open and closed blue symbols), contactless Hall effect (red open circles), C–V profiling (golden closed symbols), and Poisson–Schrödinger (P-S) computations from this work (purple open circles). Lines with no symbols are according to the formulas derived in Ref. 5 (black solid) and Ref. 4 (black dashed). Results from both the primary (dashed lines, open circles) and secondary (solid lines, closed diamonds) THz-OHE model analysis are shown for comparison. The primary analysis allows all 2DEG parameters  $N_{\rm s}$ ,  $\mu$ , and  $m^*$  to be freely fit, whereas the secondary analysis fixes  $m^*$  to the theoretical calculations (Fig. 6: hyb. + polaron + nonparabol.). Results from the primary THz-OHE analysis are replicated in the inset for better comparison.

features become more pronounced with increasing Al content x because of changes in 2DEG parameters. For smaller x values, i.e., 0.07, the THz-OHE spectra are close to zero due to lower 2DEG densities. In this case, parameters  $N_{\rm s}$ ,  $m^{\star}$ , and  $\mu$  are highly correlated. To provide a helpful comparison, a second model analysis of the THz-OHE data was performed by adopting theoretically estimated values of  $m^{\star}$  as discussed in more detail below. The results for the 2DEG properties determined by both these model approaches are presented in Figs. 4, 5, 7, and 8.

Figure 4 summarizes the sheet electron density  $N_{\rm s}$  obtained from THz-OHE, C–V, contactless Hall effect, P-S simulations, and the analytical approximations by Ambacher  $et~al.^{4,5}$  The 2DEG density depends almost linearly on the Al composition x. We find good agreement between the values obtained from the different experimental and theoretical methods. For small x, results from THz-OHE agree better with theoretical expectations and C–V profiling than do values from the contactless Hall measurements. THz-OHE values deviate more for the highest Al composition x=0.42, and depend on whether the effective mass was varied or fixed. For the contactless Hall effect measurements, results are shown only for samples with  $x\leq 0.3$  due to detection limits of the instrumentation.

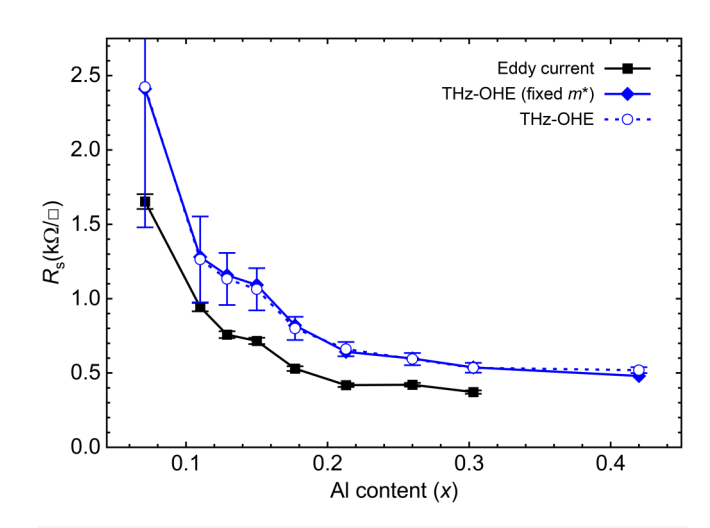


**FIG. 5.** Sheet resistance  $R_s$  obtained from THz-OHE and Eddy current measurements. For the THz-OHE results, values were calculated using  $R_s = (e\mu N_s)^{-1}$ . As in Fig. 4, results from the primary (open circles) and secondary (solid diamonds) THz-OHE analyses are shown for comparison.

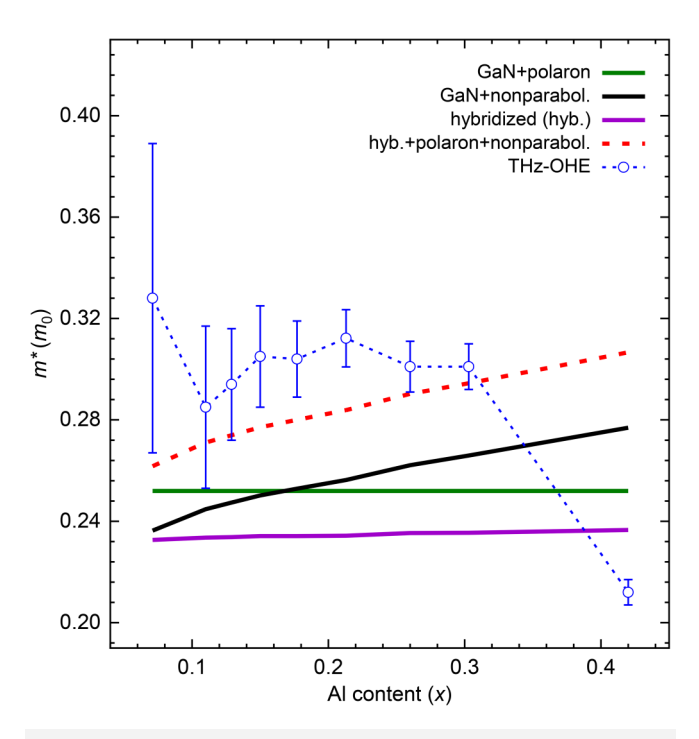


**FIG. 6.** Isotropically averaged 2DEG effective mass parameter  $m^*$  experimentally determined by THz-OHE along with theoretical similations. Simulations are based on the  $m^*$  values for bulk-like n-type  $A_x Ga_{1-x} N$  given in Ref. 29. Effective electron mass enhancement by hybridization [Eq. (5)], nonparabolicity [Eq. (6)], polaron effect [Eq. (7)], and all effects combined are shown according to the legend. Note that mass enhancement for the polaron effect is constant as a function of Al content x, whereas the enhancement due to hybridization and nonparabolicity are defined as x-dependent. Error bars for the THz-OHE results correspond to the 90% confidence interval as calculated by WVASE.

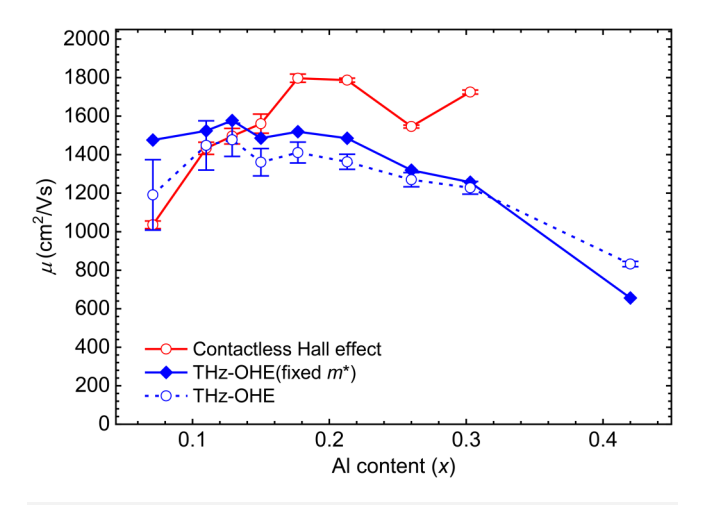


**FIG. 7.** Isotropically averaged 2DEG mobility  $\mu$  obtained by THz-OHE and contactless Hall effect measurements. As in Figs. 4 and 5, blue circles are results from THz-OHE modeling with free  $N_{\rm S}$ ,  $\mu$  and  $m^*$ , and blue diamonds the same except with  $m^*$  values fixed to theoretically calculated values (Fig. 6: hyb. + polaron + nonparabol.).

Figure 5 shows sheet resistance  $R_s$  as measured where applicable or computed from  $N_s$  and  $\mu$  via  $R_s = (e\mu N_s)^{-1}$ . A similar trend is observed for both THz-OHE and contactless Eddy current results with increasing Al content. This is primarily due to the large variation of  $N_s$ , which is directly proportional to the DC conductivity. An offset of about  $200 \, \Omega/\Box$  is noted for the Eddy current results. Results from the primary and secondary THz-OHE analyses produce nearly identical values of  $R_s$ .

Shown in Fig. 6 are results for the 2DEG effective mass as a \$\overline{\ove function of Al fraction determined by THz-OHE experiments and by theoretical simulations (hybridization, nonparabolicity, polaron effect, and all effects combined). The calculation for all combined enhancement effects is implemented by multiplying the resulting hybridized effective mass [Eq. (5)] by the enhancement ratios for nonparabolicity [Eq. (6)] and the polaron effect [Eq. (7)]. simulations for effective mass enhancement are performed using the  $m^*$  values provided in Ref. 29 for electrons in Al<sub>x</sub>Ga<sub>1-x</sub>N, which are calculated by linear interpolation between  $m_{\text{GaN}}^* = 0.232 \, m_0$  and  $m_{\text{AlN}}^* = 0.364 \, m_0$ . Although slight anisotropy may be expected for  $m^*$ , all theoretical and experimental results in Fig. 6 are presented as an isotropic average. According to our theoretical calculations for hybridization [Eq. (5)], no significant increase of m\* with Al content is expected due to penetration of the electron wavefunction into the barrier layer. However, effective mass enhancement predicted from conduction band nonparabolicity shows a much larger variation of  $m^*$  with x [Eq. (6)]. For the polaron effect, no change in  $m^*$  is calculated as defined by the model in [Eq. (7)], but rather a constant increase of 8.6% relative to  $m_{\text{GaN}}^*$ . Most of the experimentally obtained THz-OHE  $m^*$  values are near  $0.3 m_0$ , demonstrating a noticeable enhancement even beyond the various predicted values given in Fig. 6. The only exception is the data point for x = 0.42, which is closest to the GaN bulk value  $m_{GaN}^*$ .

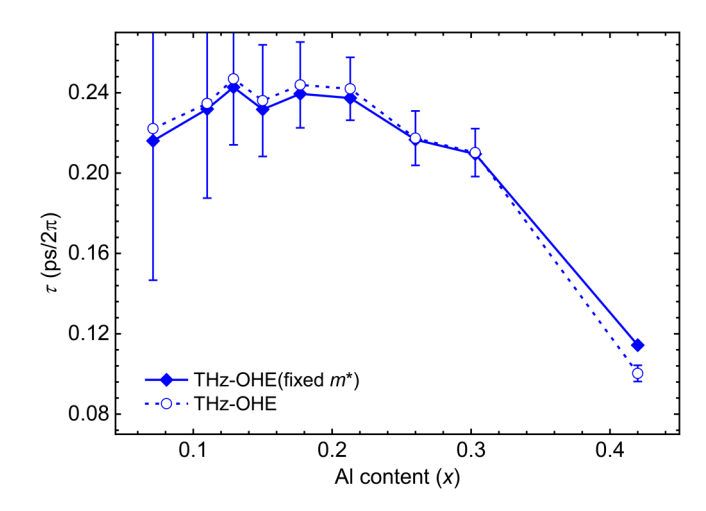


FIG. 8. Isotropically averaged electron scattering time  $\tau$  obtained by THz-OHE  $( au=\gamma_{
m p}^{-1}=\mu{\it m}^*/{\it e}).$  Symbols and color codes are the same as in Figs. 4, 5,

Figure 7 summarizes the electron mobility parameters obtained from THz-OHE and contactless Hall effect measurements. Results from THz-OHE are shown for the model approaches with either free or fixed effective mass parameters. The resulting 2DEG mobilities show a maximum near 15%-20% Al content. Mobility values from the contactless Hall measurements mimic the trend found from THz-OHE. However, the absolute values differ from those obtained by THz-OHE. Attempts to compute mobility by combining the C-V and Eddy current measurements proved unsuccessful due to large data uncertainties.

Figure 8 shows the scattering time  $\tau$  which is directly obtained from the Drude model's plasma broadening parameter after bestmatch calculation to the THz-OHE data. We observe that  $\tau$  shows a similar tendency with x as does  $\mu$ . This observation highlights a central result of this work: the decrease in 2DEG mobility with increasing Al content is mostly driven by the reduced scattering times, while the effective mass remains mostly unchanged within the uncertainty limits (except for x = 0.42).

### V. DISCUSSION

### A. 2DEG effective mass parameter

Our results on the enhancement of the effective mass at RT using the models described in Eqs. (5)-(7) are different from those previously reported at LT for similar AlGaN/GaN heterostructures. 37,39,47 Using SdH effect measurements at <10 K, Kurakin et al. found that the main effect of the 2DEG confinement on  $m^*$ was penetration of the wavefunction into the barrier layer and the subsequent hybridization between the GaN and Al<sub>x</sub>Ga<sub>1-x</sub>N effective mass.<sup>37</sup> For a penetration in the barrier of about 10%, as occurs in our structures, an increase of the effective mass parameter by  $\approx$ 15% should be expected according to Kurakin et al. However, for our HEMT structures at room temperature we find the calculated effect of hybridization rather small (<2%). The lowtemperature experiments reported in Refs. 39 and 47 demonstrated that conduction band nonparabolicity was the dominant mechanism for m\* enhancement on the investigated AlGaN/GaN HEMT structures using SdH effect and cyclotron resonance. Our theoretical calculations at room temperature show a similar result, in which conduction band nonparabolicity is responsible for the largest increase of  $m^*$  with x of 17%. For a similar Al-content/2DEG sheet density range, Ref. 39 estimates an enhancement due to nonparabolicity of  $\approx$ 10% at low temperatures. We note that magnetic field dependent nonparabolicity was not included in our simulations. However for the THz-OHE experiments, the low magnetic fields (0.6 T) should not induce a significant change in  $m^*$ .

Comparing all experimental THz-OHE results for  $m^*$  with xto our theoretical estimations (Fig. 6) demonstrates that all mechanisms of effective mass enhancement should be considered simultaneously in order to explain the larger  $m^*$  values: hybridization, nonparabolicity, and the polaron effect. Still, the experimental results are slightly larger than all combined effects, and appear rather flat overall, with the exception of the largest Al-content sample, the values remain around  $0.3m_0$ . Although the point x =0.42 is an outlier, its error bars are the smallest in the series, which is caused by the larger THz-OHE signal. A future study of higher Al content HEMT structures would be needed to confirm a downward  $m^*$  trend toward higher x values. Partial relaxation of the barrier layer through Al content change as well as a partially populated second subband may also play a role in explaining the lower  $m^*$  for this higher Al content sample. However we note that in our THz-OHE analysis, no indication was found for the existence of a secondary charge carrier species within the 2DEGs.

vious THz-OHE<sup>33</sup> and THz-TDS (via 2D plasmon resonance)<sup>42</sup> of Studies have measured a strong temperature. 2DEG effective mass in similar AlGaN/GaN heterostructures. Both studies found an effective mass close to  $m_{\text{GaN}}^*$  at low temperatures  $(m^* \approx 0.22 m_0)$ , but at room temperature determined larger values of  $m^* \approx 0.36m_0$ . This is in line with the larger room temperature 2DEG effective masses reported in this work of  $\approx 0.3 m_0$ . Even though values of  $0.3m_0$  can be explained using the enhancement mechanisms here (hybridization, nonparabolicity, polaron effect), the investigations in Refs. 33 and 42 show that further work must be done before this strong temperature-dependent enhancement of  $m^*$  is understood. These comparisons demonstrate that HEMT structure temperature is important to consider in view of the 2DEG effective mass.

### B. 2DEG mobility parameter

Regarding our experimentally determined 2DEG mobilities, results from both THz-OHE and contactless Hall effect measurements are relatively low due to the absence of an ≈1 nm AlN interlayer between the AlGaN barrier and GaN buffer layers, which is commonly incorporated to reduce interface scattering. In a previous work, we have demonstrated a contactless Hall effect mobility of  $(2370 \pm 25)$  cm<sup>2</sup>/V s for an AlGaN/AlN/GaN HEMT structure at room temperature.<sup>23</sup> As mentioned above, the HEMT structures studied in this work were intentionally grown without a thin AlN interlayer. Although the experimental errors become larger with

decreasing Al content, it can be discerned that both the THz-OHE and contactless Hall effect mobilities reach a maximum near  $x \approx 0.17$ . This is consistent with many previous studies on similar AlGaN/GaN-based HEMT structures. 2,7,9,15,73,7

A notable feature of our experimental mobilities is that the results from THz-OHE and contactless Hall effect differ in their absolute values. Near an Al content of  $x \approx 0.2$ , mobility values from THz-OHE are approximately 400 cm<sup>2</sup>/V s lower than for the contactless Hall effect. Both of these measurement techniques assume that the 2DEG response can be described by the classical Drude model. In the simple Drude transport picture, mobilities extracted by THz-OHE and contactless Hall effect should be identical. Since our results demonstrate that this is not the case, we suggest one possible implication may be that more complex transport mechanisms are at work. Therefore, we emphasize the importance of using multiple characterization methods, since we observe such a difference between THz-OHE and contactless Hall effect mobilities.

### C. 2DEG scattering time and effective mass separation

Since the Drude mobility parameter can be written as  $\mu = \tau/(em^*)$ , it is beneficial to view the scattering time  $\tau$  and effective mass  $m^*$  separately, in order to better understand the factors involved in 2DEG mobility reduction. For example, we can examine the results for x = 0.13 and x = 0.42, which correspond to the highest,  $(1477 \pm 86)$  cm<sup>2</sup>/V s, and lowest,  $(832 \pm 14)$  cm<sup>2</sup>/V s, mobilities from the primary THz-OHE analysis, respectively. This distinction between  $\tau$  and  $m^*$  determines which of the two is mostly responsible for limiting the mobility for the HEMT structure with x = 0.42, relative to x = 0.13. For the 2DEG scattering time (Fig. 8), a reduction of  $\tau$  by 59% is seen from x = 0.13 to x = 0.42, which contributes to a mobility reduction of 59% due to their directly proportional relationship. For the 2DEG effective mass (Fig. 6), a decrease of  $m^*$  by 28% is seen, which contributes to a mobility increase of 39% due to their inverse relationship. Therefore, over the Al content range of x = 0.13 to x = 0.42 we conclude that the limitation of our THz-OHE mobilities is from the decrease in 2DEG scattering time, whereas the decrease in effective mass actually contributes to increasing  $\mu$ .

To the best of our knowledge, there exist no previous reports of both the 2DEG scattering time and effective mass obtained at room temperature for AlGaN/GaN-based HEMT structures. However, our room temperature THz-OHE results are quite similar to a previously reported Drude scattering time  $\tau_0$  deduced from magnetoresistance and SdH effect measurements at low temperatures. 16 For this 2DEG within a modulated doped Al<sub>0.25</sub>Ga<sub>0.75</sub>N/ GaN heterostructure,  $\tau_0 = 0.26 \,\mathrm{ps}$  was given by Ref. 16, which is comparable to  $\tau \approx 0.22 \, \text{ps}$  found for our HEMT structure with x = 0.26.

### VI. CONCLUSION

In summary, we have studied a series of Al<sub>x</sub>Ga<sub>1-x</sub>N/GaN heterostructures with Al composition of the barrier x varying between 0.07 and 0.42 in order to assess their 2DEG parameters. The THz-OHE measurements and analysis yield room temperature values for 2DEG sheet density, effective mass, and mobility parameters, which also allows to evaluate the Drude scattering time. We find the 2DEG sheet densities increase with x according to theoretical expectations, mobility mostly decreasing for large x, and the effective mass generally increased with respect to free electrons in bulk GaN. According to our theoretical calculations, the larger experimentally determined electron effective masses at room temperature can be explained by the combined effects of the electron wavefunction penetration into the barrier, conduction band nonparabolicity, and polaron enhancement. From the scattering time and effective mass separation provided by the THz-OHE results, we find that the decreasing 2DEG mobility from x = 0.13to x = 0.42 is driven by a decrease in scattering time. This investigation highlights the importance of characterizing such HEMT structures near the frequencies and temperatures at which they will operate in modern electronic devices.

### SUPPLEMENTARY MATERIAL

See the supplementary material for additional results and data regarding the AFM, SE, XRD-RSM, THz-OHE, and C-V characterizations, as well as the Poisson-Schrödinger simulations.

### **ACKNOWLEDGMENTS**

This work was performed within the framework of the Competence Center for III-Nitride Technology, C3NiT—Janzén, og supported by the Swedish Governmental Agency for Innovation Systems (VINNOVA) under the Competence Center Program Grant No. 2022-03139. Lund University, Linköping University, Chalmers University of Technology, Ericsson, Epiluvac, FMV, Gotmic, Hexagem, Hitachi Energy, On Semiconductor, Region 5 Skåne, SAAB, SweGaN, Volvo Cars, and UMS are acknowledged. We further acknowledge support from the Swedish Research Council VR under Award Nos. 2016-00889 and 2022-04812, Swedish Foundation for Strategic Research under Grant Nos. RIF14-055, EM16-0024, and STP19-0008, and the Swedish Government Strategic Research Area in Materials Science on Functional Materials at Linköping University, Faculty Grant SFO Mat LiU No. 2009-00971. The KAW Foundation is also acknowledged for the support of the Linköping Electron Microscopy Laboratory. P. O. Å. Persson acknowledges ARTEMI, the Swedish National Infrastructure in Advanced Electron Microscopy, through funding from the Swedish Research Council and the Foundation for Strategic Research (Grant No. 2021-00171 and RIF21-0026). M.S. acknowledges support of this work in part by the National Science Foundation (NSF) under Award Nos. NSF DMR 1808715 and NSF/EPSCoR RII Track-1: Emergent Quantum Materials and Technologies (EQUATE), Award No. OIA-2044049, by Air Force Office of Scientific Research under Award Nos. FA9550-18-1-0360, FA9550-19-S-0003, and FA9550-21-1-0259, by the Knut and Alice Wallenbergs Foundation award "Wide-bandgap semiconductors for next generation quantum components," by the University of Nebraska Foundation, and by the J. A. Woollam Foundation. S.K. is grateful to Mario Ancona for a helpful discussion on densitygradient theory.

### **AUTHOR DECLARATIONS**

### Conflict of Interest

The authors have no conflicts to disclose.

### Author Contributions

Sean Knight: Formal analysis (supporting); Investigation (supporting); Writing - original draft (equal). Steffen Richter: Formal analysis (lead); Investigation (equal); Writing - original draft (equal). Alexis Papamichail: Formal analysis (supporting); Investigation (equal). Philipp Kühne: Formal analysis (supporting). Nerijus Armakavicius: Formal analysis (supporting). Shiqi Guo: Formal analysis (supporting). Axel R. Persson: Formal analysis (supporting); Investigation (supporting). Vallery Stanishev: Formal analysis (supporting). Viktor Rindert: Formal analysis (supporting). Per O. Å. Persson: Supervision (supporting); Writing - review & editing (supporting). Plamen P. Paskov: Formal analysis (supporting); Writing - review & editing (equal). Mathias Schubert: Writing review & editing (equal). Vanya Darakchieva: Conceptualization (lead); Funding acquisition (lead); Resources (lead); Supervision (lead); Writing - review & editing (equal).

### DATA AVAILABILITY

The data that support the findings of this study are available from the corresponding authors upon reasonable request.

### REFERENCES

- <sup>1</sup>J. S. Moon, J. Wong, B. Grabar, M. Antcliffe, P. Chen, E. Arkun, I. Khalaf, A. Corrion, J. Chappell, N. Venkatesan, and P. Fay, "360 GHz f<sub>MAX</sub> gradedchannel AlGaN/GaN HEMTs for mmW low-noise applications," IEEE Electron Device Lett. 41, 1173 (2020).
- <sup>2</sup>O. Ambacher, J. Smart, J. R. Shealy, N. G. Weimann, K. Chu, M. Murphy, W. J. Schaff, L. F. Eastman, R. Dimitrov, L. Wittmer, M. Stutzmann, W. Rieger, and J. Hilsenbeck, "Two-dimensional electron gases induced by spontaneous and piezoelectric polarization charges in N- and Ga-face AlGaN/GaN heterostructures," J. Appl. Phys. 85, 3222 (1999).
- <sup>3</sup>O. Ambacher, B. Foutz, J. Smart, J. R. Shealy, N. G. Weimann, K. Chu, M. Murphy, A. J. Sierakowski, W. J. Schaff, L. F. Eastman, R. Dimitrov, A. Mitchell, and M. Stutzmann, "Two dimensional electron gases induced by spontaneous and piezoelectric polarization in undoped and doped AlGaN/GaN heterostructures," J. Appl. Phys. 87, 334 (2000).
- <sup>4</sup>O. Ambacher, J. Majewski, C. Miskys, A. Link, M. Hermann, M. Eickhoff, M. Stutzmann, F. Bernardini, V. Fiorentini, V. Tilak, B. Schaff, and L. F. Eastman, "Pyroelectric properties of Al(In)GaN/GaN hetero- and quantum well structures," J. Phys.: Condens. Matter 14, 3399 (2002).
- <sup>5</sup>O. Ambacher, B. Christian, M. Yassine, M. Baeumler, S. Leone, and R. Quay, "Polarization induced interface and electron sheet charges of pseudomorphic ScAlN/GaN, GaAlN/GaN, InAlN/GaN, and InAlN/InN heterostructures," J. Appl. Phys. 129, 204501 (2021).
- <sup>6</sup>S.-H. Yoo, M. Todorova, J. Neugebauer, and C. G. Van de Walle, "Microscopic origin of polarization charges at GaN/(Al,Ga)N interfaces," Phys. Rev. Appl. 19,
- 7S. Keller, G. Parish, P. T. Fini, S. Heikman, C.-H. Chen, N. Zhang, S. P. DenBaars, U. K. Mishra, and Y.-F. Wu, "Metalorganic chemical vapor deposition of high mobility AlGaN/GaN heterostructures," J. Appl. Phys. 86, 5850
- <sup>8</sup>I. P. Smorchkova, C. R. Elsass, J. P. Ibbetson, R. Vetury, B. Heying, P. Fini, E. Haus, S. P. DenBaars, J. S. Speck, and U. K. Mishra, "Polarization-induced

- charge and electron mobility in AlGaN/GaN heterostructures grown by plasma-assisted molecular-beam epitaxy," J. Appl. Phys. **86**, 4520 (1999). <sup>9</sup>Z. Bougrioua, J. L. Farvacque, I. Moerman, and F. Carosella, "2DEG mobility in
- AlGaN-GaN structures grown by LP-MOVPE," Phys. Status Solidi B 228, 625
- 10 K. A. Mkhoyan, J. Silcox, Z. Yu, W. J. Schaff, and L. F. Eastman, "Formation of a quasi-two-dimensional electron gas in GaN/Al<sub>x</sub>Ga<sub>1-x</sub>N heterostructures with diffuse interfaces," J. Appl. Phys. 95, 1843 (2004).
- 11 M. Miyoshi, T. Egawa, and H. Ishikawa, "Structural characterization of strained AlGaN layers in different Al content AlGaN/GaN heterostructures and its effect on two-dimensional electron transport properties," J. Vac. Sci. Technol. B 23,
- 12S. W. Kaun, P. G. Burke, M. H. Wong, E. C. H. Kyle, U. K. Mishra, and J. S. Speck, "Effect of dislocations on electron mobility in AlGaN/GaN and AlGaN/AlN/GaN heterostructures," Appl. Phys. Lett. 101, 262102 (2012).
- 13G. Jiang, Y. Lv, Z. Lin, Y. Yang, and Y. Liu, "The influence of Al composition in AlGaN barrier layer on polarization Coulomb field scattering in AlGaN/GaN heterostructure field-effect transistors," Phys. E 127, 114576 (2021).
- <sup>14</sup>A. Yamada, J. Yaita, N. Nakamura, and J. Kotani, "Low-sheet-resistance high-electron-mobility transistor structures with strain-controlled high-Al-composition AlGaN barrier grown by MOVPE," J. Cryst. Growth 560-561, 126046
- 15 V. M. Polyakov, V. Cimalla, V. Lebedev, K. Köhler, S. Müller, P. Waltereit, and O. Ambacher, "Impact of Al content on transport properties of two-dimensional electron gas in GaN/Al<sub>x</sub>Ga<sub>1-x</sub>N/GaN heterostructures," Appl. Phys. Lett. 97, 142112 (2010).
- 16A. F. Braña, C. Diaz-Paniagua, F. Batallan, J. A. Garrido, E. Muñoz, and F. Omnes, "Scattering times in AlGaN/GaN two-dimensional electron gas from magnetoresistance measurements," J. Appl. Phys. 88, 932 (2000).
- 17 T. Wang, J. Bai, S. Sakai, Y. Ohno, and H. Ohno, "Magnetotransport studies of AlGaN/GaN heterostructures grown on sapphire substrates: Effective mass and scattering time," Appl. Phys. Lett. **76**, 2737 (2000).

  18 L. Hsu and W. Walukiewicz, "Electron mobility in Al<sub>x</sub>Ga<sub>1-x</sub>N/GaN heterostructures," Phys. Rev. B **56**, 1520–1528 (1997).
- structures," Phys. Rev. B 56, 1520-1528 (1997).
- 19X. Wang, G. Hu, Z. Ma, J. Ran, C. Wang, H. Xiao, J. Tang, J. Li, J. Wang, S. Xiao, J. Tang, J. Xiao, J. Xia Y. Zeng, J. Li, and Z. Wang, "AlGaN/AlN/GaN/SiC HEMT structure with high mobility GaN thin layer as channel grown by MOCVD," J. Cryst. Growth 298,
- 20 J.-T. Chen, I. Persson, D. Nilsson, C.-W. Hsu, J. Palisaitis, U. Forsberg, P. O. Å. Persson, and E. Janzén, "Room-temperature mobility above 2200 cm<sup>2</sup>/ V s of two-dimensional electron gas in a sharp-interface AlGaN/GaN heterostructure," Appl. Phys. Lett. 106, 251601 (2015).
- <sup>21</sup>N. Armakavicius, J.-T. Chen, T. Hofmann, S. Knight, P. Kühne, D. Nilsson, U. Forsberg, E. Janzén, and V. Darakchieva, "Properties of two-dimensional electron gas in AlGaN/GaN HEMT structures determined by cavity-enhanced THz optical Hall effect," Phys. Status Solidi C 13, 369 (2016).
- <sup>22</sup>J. Chu, Q. Wang, L. Jiang, C. Feng, W. Li, H. Liu, H. Xiao, and X. Wang, "Room temperature 2DEG mobility above 2350 cm<sup>2</sup>/V s in AlGaN/GaN HEMT
- grown on GaN substrate," J. Electron. Mater. **50**, 2630 (2021). **23**A. Papamichail, A. Persson, S. Richter, P. Kühne, V. Stanishev, P. Å. Persson, R. Ferrand-Drake Del Castillo, M. Thorsell, H. Hjelmgren, P. Paskov, N. Rorsman, and V. Darakchieva, "Tuning composition in graded AlGaN channel HEMTs toward improved linearity for low-noise radio-frequency amplifiers," Appl. Phys. Lett. 122, 153501 (2023).
- 24Y. S. Huang and F. H. Pollak, "Non-destructive, room temperature characterization of wafer-sized III-V semiconductor device structures using contactless electromodulation and wavelength-modulated surface photovoltage spectroscopy," Phys. Status Solidi A 202, 1193 (2005).
- 25 R. Kudrawiec, M. Syperek, M. Motyka, J. Misiewicz, R. Paszkiewicz, B. Paszkiewicz, and M. Tlaczala, "Contactless electromodulation spectroscopy of AlGaN/GaN heterostructures with a two-dimensional electron gas: A comparison of photoreflectance and contactless electroreflectance," J. Appl. Phys. 100, 013501 (2006).

- <sup>26</sup>M. Schubert, P. Kühne, V. Darakchieva, and T. Hofmann, "Optical Hall effect-Model description: Tutorial," J. Opt. Soc. Am. A 33, 1553 (2016).
- <sup>27</sup>Y. Turkulets and I. Shalish, "Contactless method to measure 2DEG charge density and band structure in HEMT structures," IEEE J. Electron Devices Soc. 6, 703 (2018).
- <sup>28</sup>T. Hofmann, V. Darakchieva, B. Monemar, H. Lu, W. J. Schaff, and M. Schubert, "Optical Hall effect in hexagonal InN," J. Electron. Mater. 37, 611
- <sup>29</sup>S. Schöche, T. Hofmann, D. Nilsson, A. Kakanakova-Georgieva, E. Janzén, P. Kühne, K. Lorenz, M. Schubert, and V. Darakchieva, "Infrared dielectric functions, phonon modes, and free-charge carrier properties of high-Al-content Al<sub>x</sub>Ga<sub>1-x</sub>N alloys determined by mid infrared spectroscopic ellipsometry and optical Hall effect," J. Appl. Phys. 121, 205701 (2017).
- 30N. Armakavicius, V. Stanishev, S. Knight, P. Kühne, M. Schubert, and V. Darakchieva, "Electron effective mass in In<sub>0.33</sub>Ga<sub>0.67</sub>N determined by midinfrared optical Hall effect," Appl. Phys. Lett. 112, 082103 (2018).
- 31 S. Knight, A. Mock, R. Korlacki, V. Darakchieva, B. Monemar, Y. Kumagai, K. Goto, M. Higashiwaki, and M. Schubert, "Electron effective mass in Sn-doped monoclinic single crystal β-gallium oxide determined by mid-infrared optical Hall effect," Appl. Phys. Lett. 112, 012103 (2018).
- 32 S. Knight, T. Hofmann, C. Bouhafs, N. Armakavicius, P. Kühne, V. Stanishev, I. G. Ivanov, R. Yakimova, S. Wimer, M. Schubert, and V. Darakchieva, "In situ terahertz optical Hall effect measurements of ambient effects on free charge carrier properties of epitaxial graphene," Sci. Rep 7, 5151 (2017).
- 33T. Hofmann, P. Kühne, S. Schöche, J.-T. Chen, U. Forsberg, E. Janzén, N. B. Sedrine, C. M. Herzinger, J. A. Woollam, M. Schubert, and V. Darakchieva, "Temperature dependent effective mass in AlGaN/GaN high electron mobility transistor structures," Appl. Phys. Lett. 101, 192102 (2012).
- <sup>34</sup>P. Kühne, N. Armakavicius, A. Papamichail, D. Q. Tran, V. Stanishev, M. Schubert, P. P. Paskov, and V. Darakchieva, "Enhancement of 2DEG effective mass in AlN/Al<sub>0.78</sub>Ga<sub>0.22</sub>N high electron mobility transistor structure determined by THz optical Hall effect," Appl. Phys. Lett. 120, 253102 (2022).
- 35A. Kasic, M. Schubert, S. Einfeldt, D. Hommel, and T. E. Tiwald, "Free-carrier and phonon properties of n- and p-type hexagonal GaN films measured by infrared ellipsometry," Phys. Rev. B **62**, 7365 (2000). <sup>36</sup>P. Perlin, E. Litwin-Staszewska, B. Suchanek, W. Knap, J. Camassel, T. Suski,
- R. Piotrzkowski, I. Grzegory, S. Porowski, E. Kaminska, and J. C. Chervin, "Determination of the effective mass of GaN from infrared reflectivity and Hall effect," Appl. Phys. Lett. **68**, 1114 (1996). <sup>37</sup>A. M. Kurakin, S. A. Vitusevich, S. V. Danylyuk, H. Hardtdegen, N. Klein,
- Z. Bougrioua, A. V. Naumov, and A. E. Belyaev, "Quantum confinement effect on the effective mass in two-dimensional electron gas of AlGaN/GaN heterostructures," J. Appl. Phys. **105**, 073703 (2009). **38**T. Ando, "Self-consistent results for a  $GaAs/Al_xGa_{1-x}As$  heterojunction.
- I. Subband structure and light-scattering spectra," J. Phys. Soc. Jpn. 51, 3893
- <sup>39</sup>W. Knap, S. Contreras, H. Alause, C. Skierbiszewski, J. Camassel, M. Dyakonov, J. L. Robert, J. Yang, Q. Chen, M. A. Khan, M. L. Sadowski, S. Huant, F. H. Yang, M. Goiran, J. Leotin, and M. S. Shur, "Cyclotron resonance and quantum Hall effect studies of the two-dimensional electron gas confined at the GaN/AlGaN interface," Appl. Phys. Lett. 70, 2123 (1997).
- 40 V. V. Korotyeyev, V. A. Kochelap, V. V. Kaliuzhnyi, and A. E. Belyaev, "High-frequency conductivity and temperature dependence of electron effective mass in AlGaN/GaN heterostructures," Appl. Phys. Lett. 120, 252103 (2022).
- <sup>41</sup>D. R. Hang, C.-T. Liang, C. F. Huang, Y. H. Chang, Y. F. Chen, H. X. Jiang, and J. Y. Lin, "Effective mass of two-dimensional electron gas in an Al<sub>0.2</sub>Ga<sub>0.8</sub>N/ GaN heterojunction," Appl. Phys. Lett. 79, 66 (2001).
- 42D. Pashnev, V. V. Korotyeyev, J. Jorudas, T. Kaplas, V. Janonis, A. Urbanowicz, and I. Kašalynas, "Experimental evidence of temperature dependent effective mass in AlGaN/GaN heterostructures observed via THz spectroscopy of 2D plasmons," Appl. Phys. Lett. 117, 162101 (2020).
- 43D. Pashnev, V. V. Korotyeyev, J. Jorudas, A. Urbanowicz, P. Prystawko, V. Janonis, and I. Kašalynas, "Investigation of electron effective mass in AlGaN/

- GaN heterostructures by THz spectroscopy of drude conductivity," IEEE Trans. Electron Devices 69, 3636 (2022).
- <sup>44</sup>F. Sonmez, S. Ardali, S. B. Lisesivdin, T. Malin, V. Mansurov, K. Zhuravlev, and E. Tiras, "The effect of barrier layers on 2D electron effective mass in Al<sub>0.3</sub>Ga<sub>0.7</sub>N/AlN/GaN heterostructures," J. Phys.: Condens. Matter 33, 255501 (2021).
- 45 A. Saxler, P. Debray, R. Perrin, S. Elhamri, W. C. Mitchel, C. R. Elsass, I. P. Smorchkova, B. Heying, E. Haus, P. Fini, J. P. Ibbetson, S. Keller, P. M. Petroff, S. P. DenBaars, U. K. Mishra, and J. S. Speck, "Characterization of an AlGaN/GaN two-dimensional electron gas structure," J. Appl. Phys. 87, 369
- 46S. Syed, J. B. Heroux, Y. J. Wang, M. J. Manfra, R. J. Molnar, and H. L. Stormer, "Nonparabolicity of the conduction band of wurtzite GaN," Appl. Phys. Lett. 83, 4553 (2003).
- 47N. Tang, B. Shen, M. J. Wang, Z. J. Yang, K. Xu, G. Y. Zhang, T. Lin, B. Zhu, W. Z. Zhou, and J. H. Chu, "Effective mass of the two-dimensional electron gas and band nonparabolicity in Al<sub>x</sub>Ga<sub>1-x</sub>N/GaN heterostructures," Appl. Phys. Lett. 88, 172115 (2006).
- 48 M. K. Mishra, R. Manchanda, S. Lamba, O. P. Thakur, R. K. Sharma, and R. Muralidharan, "On the determination of electron effective mass in 2DEGs in gallium nitride HEMT structures," in Physics of Semiconductor Devices, edited by V. K. Jain and A. Verma (Springer, 2014), p. 99.
- 49L. W. Wong, S. J. Cai, R. Li, K. Wang, H. W. Jiang, and M. Chen, "Magnetotransport study on the two-dimensional electron gas in AlGaN/GaN heterostructures," Appl. Phys. Lett. 73, 1391 (1998).
- 50 L. L. Lev, I. O. Maiboroda, M.-A. Husanu, E. S. Grichuk, N. K. Chumakov, I. S. Ezubchenko, I. A. Chernykh, X. Wang, B. Tobler, T. Schmitt, M. L. Zanaveskin, V. G. Valeyev, and V. N. Strocov, "k-space imaging of anisotropic 2D electron gas in GaN/GaAlN high-electron-mobility transistor heterostructures," Nat. Commun. 9, 2653 (2018).
- <sup>51</sup>H. Fujiwara, Spectroscopic Ellipsometry: Principles and Applications (John Wiley & Sons, 2007). Wiley & Sons, 2007).
- 52 M. Schubert, T. Hofmann, and C. M. Herzinger, "Generalized far-infrared magneto-optic ellipsometry for semiconductor layer structures: Determination of free-carrier effective-mass, mobility, and concentration parameters in n-type 8 GaAs," J. Opt. Soc. Am. 20, 347-356 (2003).
- 553K. B. Rodenhausen and M. Schubert, "Virtual separation approach to study porous ultra-thin films by combined spectroscopic ellipsometry and quartz & crystal microbalance methods," Thin Solid Films **519**, 2772 (2011).
- J. Lindhard, Kgl. Danske Videnskab. Selskab, Mat.-Fys. Medd. 28 (1954).
- 55A. F. J. Levi, Essential Electron Transport for Device Physics (AIP Publishing LLC, Melville, 2020).
- 56W. S. Weiglhofer and A. Lakhtakia, Introduction to Complex Mediums for Optics and Electromagnetics (SPIE, Bellingham, 2003).
- <sup>57</sup>S. Knight, S. Schöche, V. Darakchieva, P. Kühne, J.-F. Carlin, N. Grandjean, C. M. Herzinger, M. Schubert, and T. Hofmann, "Cavity-enhanced optical Hall effect in two-dimensional free charge carrier gases detected at terahertz frequencies," Opt. Lett. 40, 2688 (2015).
- 58 S. Knight, S. Schöche, P. Kühne, T. Hofmann, V. Darakchieva, and M. Schubert, "Tunable cavity-enhanced terahertz frequency-domain optical Hall effect," Rev. Sci. Instrum. 91, 083903 (2020).
- 59D. Nguyen, K. Hogan, A. Blew, and M. Cordes, "Improved process control, lowered costs and reduced risks through the use of non-destructive mobility and sheet carrier density measurements on GaAs and GaN wafers," J. Cryst. Growth 272, 59-64 (2004).
- 60G. L. Snider, see https://www3.nd.edu/~gsnider/ for "1D Poisson—A Band Diagram Calculator, ver. beta 8k."
- <sup>61</sup>I. Tan, G. L. Snider, L. D. Chang, and E. L. Hu, "A self-consistent solution of Schrödinger-Poisson equations using a nonuniform mesh," J. Appl. Phys. 68, 4071-4076 (1990).
- 62M. Grundmann, The Physics of Semiconductors, 2nd ed. (Springer, 2010).
- 63S. Adachi, Properties of Group-IV, III-V and II-VI Semiconductors (John Wiley & Sons, 2009).

- <sup>64</sup>F. Oehler, M. E. Vickers, M. J. Kappers, C. J. Humphreys, and R. A. Oliver, "Fundamentals of X-ray diffraction characterisation of strain in GaN based compounds," Jpn. J. Appl. Phys. **52**, 08JB29 (2013).
  <sup>65</sup>V. Darakchieva, M. Beckers, M.-Y. Xie, L. Hultman, B. Monemar, J.-F. Carlin,
- <sup>65</sup>V. Darakchieva, M. Beckers, M.-Y. Xie, L. Hultman, B. Monemar, J.-F. Carlin, E. Feltin, M. Gonschorek, and N. Grandjean, "Effects of strain and composition on the lattice parameters and applicability of Vegard's rule in Al-rich  $Al_{1-x}In_xN$  films grown on sapphire," J. Appl. Phys. **103**, 103513 (2008).
- <sup>66</sup>P. Kühne, N. Armakavicius, V. Stanishev, C. M. Herzinger, M. Schubert, and V. Darakchieva, "Advanced terahertz frequency-domain ellipsometry instrumentation for *in situ* and *ex situ* applications," IEEE Trans. Terahertz Sci. Technol. 8, 257–270 (2018).
- <sup>67</sup>P. Kühne, C. M. Herzinger, M. Schubert, J. A. Woollam, and T. Hofmann, "Invited article: An integrated mid-infrared, far-infrared, and terahertz optical Hall effect instrument," Rev. Sci. Instrum. 85, 071301 (2014).
- <sup>68</sup>Lehighton Electronics, Inc., "Device and handling system for references measurement of mobility and sheet charge density," U.S. patent 8.207,748 B2 (26 June, 2012).
- 69 R. P. Tompkins and D. Nguyen, "Contactless mobility, carrier density, and sheet resistance measurements on Si, GaN, and AlGaN/GaN high electron

- mobility transistor (HEMT) wafers," Technical Report (Army Research Lab Adelphi MD Sensors and Electron Devices Directorate, 2015). **70**T. Metzger, R. Höpler, E. Born, O. Ambacher, M. Stutzmann, R. Stömmer,
- 70 T. Metzger, R. Höpler, E. Born, O. Ambacher, M. Stutzmann, R. Stömmer, M. Schuster, H. Göbel, S. Christiansen, M. Albrecht, and H. P. Strunk, "Defect structure of epitaxial GaN films determined by transmission electron microscopy and triple-axis x-ray diffractometry," Philos. Mag. A 77, 1013–1025 (1998).
- <sup>71</sup>V. Srikant, J. S. Speck, and D. R. Clarke, "Mosaic structure in epitaxial thin films having large lattice mismatch," J. Appl. Phys. **82**, 4286–4295 (1997).
- <sup>72</sup>K. Abgaryan, I. Mutigullin, and D. Reviznikov, "Theoretical investigation of 2DEG concentration and mobility in the AlGaN/GaN heterostructures with various Al concentrations," Phys. Status Solidi C 12, 1376–1382 (2015).
- <sup>73</sup>K. Köhler, S. Müller, P. Waltereit, L. Kirste, H. P. Menner, W. Bronner, and R. Quay, "Growth and electrical properties of  $Al_xGa_{1-x}N/GaN$  heterostructures with different Al-content," Phys. Status Solidi A **206**, 2652–2657 (2009).
- <sup>74</sup>V. M. Polyakov, F. Schwierz, I. Cimalla, M. Kittler, B. Lübbers, and A. Schober, "Intrinsically limited mobility of the two-dimensional electron gas in gated AlGaN/GaN and AlGaN/AlN/GaN heterostructures," J. Appl. Phys. 106, 023715 (2009).